Supplement

Three decades of permafrost seismic velocity variations from ambient noise at the SPITS array, Svalbard

Konstantinos Kalaitzis, Andreas Köhler, Charlotte Bruland, and Alfred Hanssen

Abstract. Supporting figures for the spectral analysis, frequency–wavenumber results, correlation processing, stacking tests, and relative seismic velocity variations reported in the main article.

S1 Probabilistic power spectral density

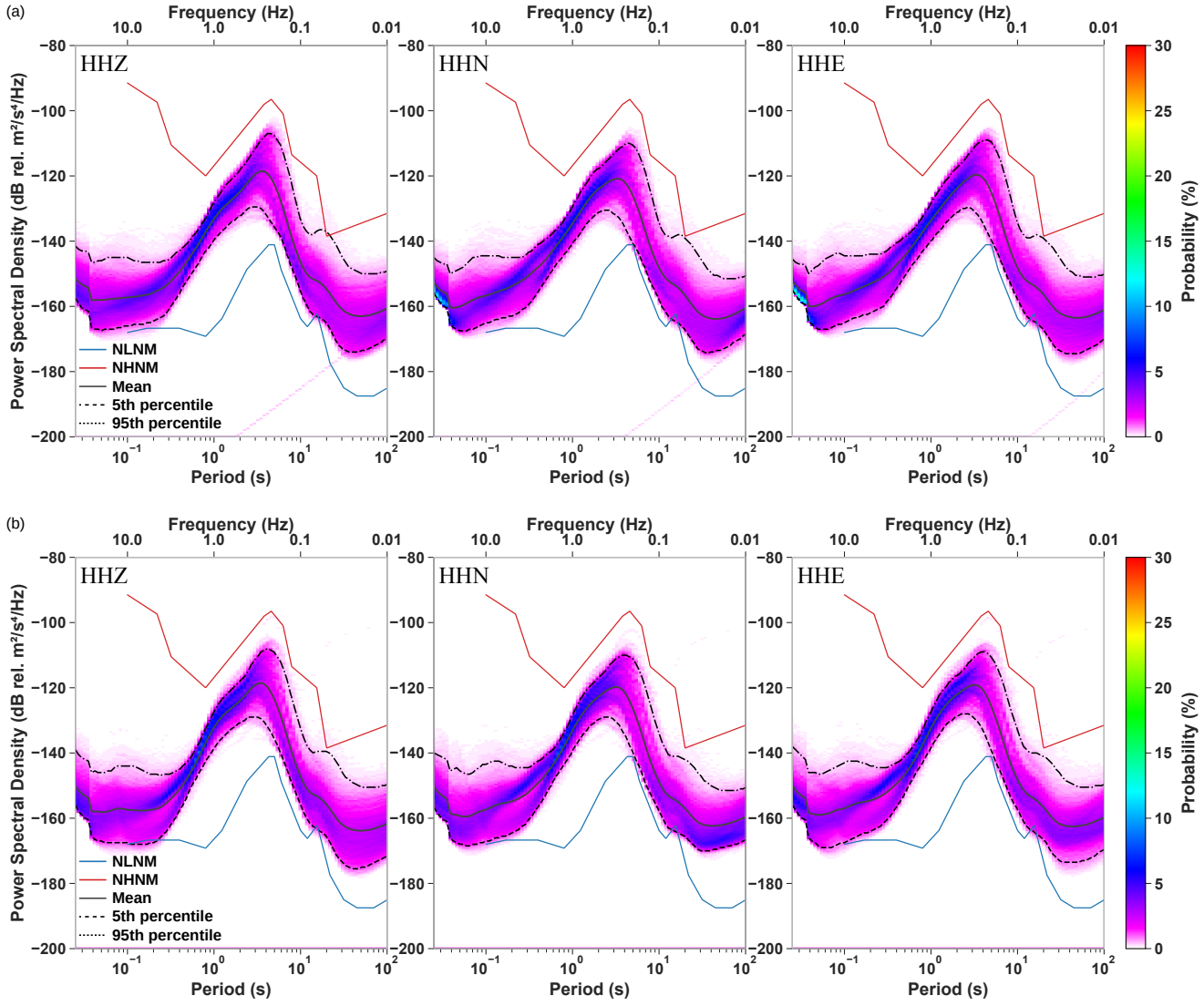


Figure S1. Multitaper PPSD. **(a)** Station SPB2 (2025). **(b)** Station SPA0 (2016). Peterson NLNM and NHNM reference models, mean, and percentile PSD traces are shown in the legend.

S2 High-frequency diurnal modulation

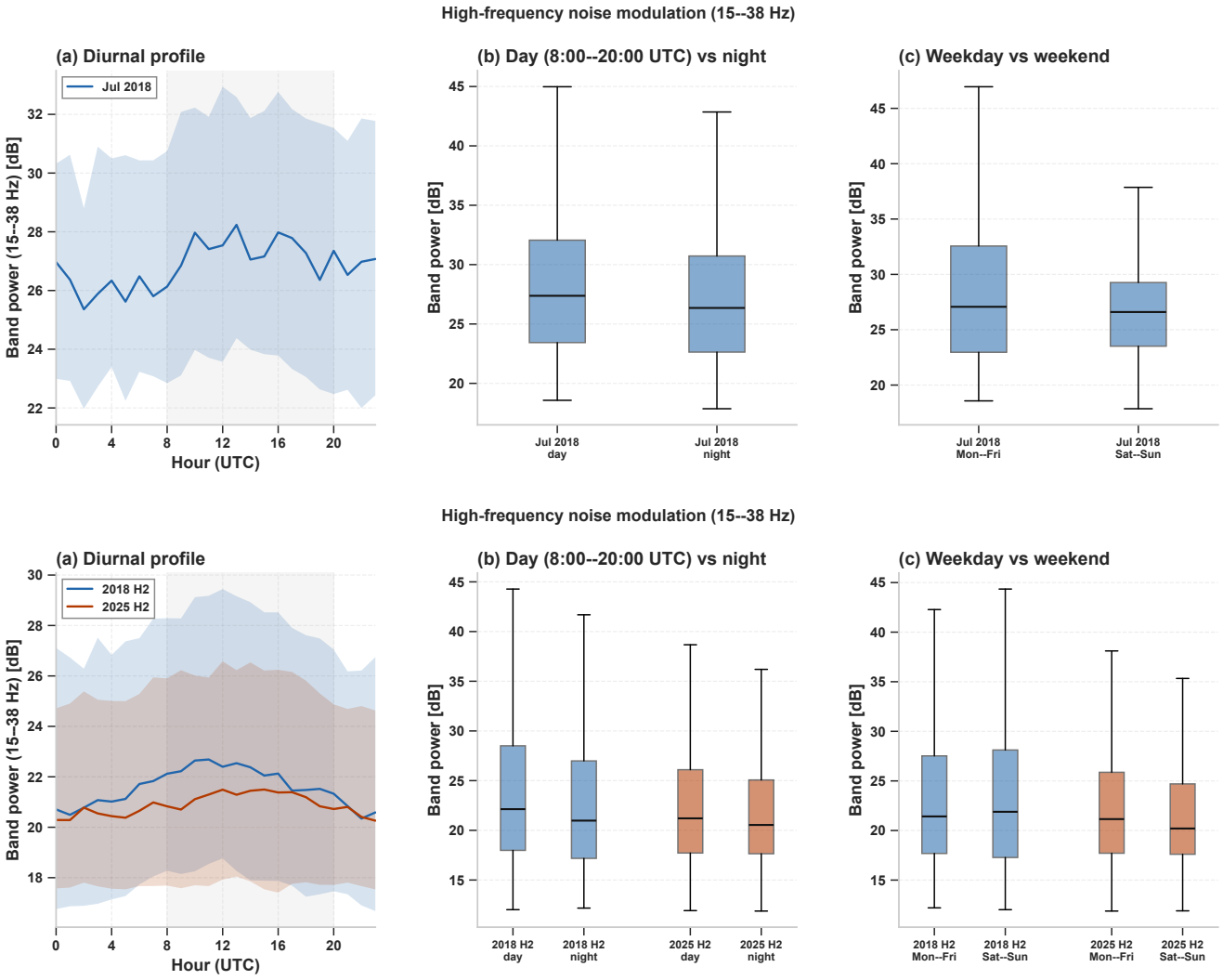


Figure S2. High-frequency noise modulation in the 15 Hz to 38 Hz band (DPSS band power on HHZ; 60 s windows). Each row shows the diurnal UTC profile (left), day (08:00–20:00 UTC) versus night boxplots (centre), and weekday versus weekend boxplots (right). **(a)** SPB2, July 2018. **(b)** SPB2, Jul–Dec 2018 (blue; Gruve 7 peak production) versus Jul–Dec 2025 (brown; coal production ceased 30 June 2025).

S3 F–K power map and histogram

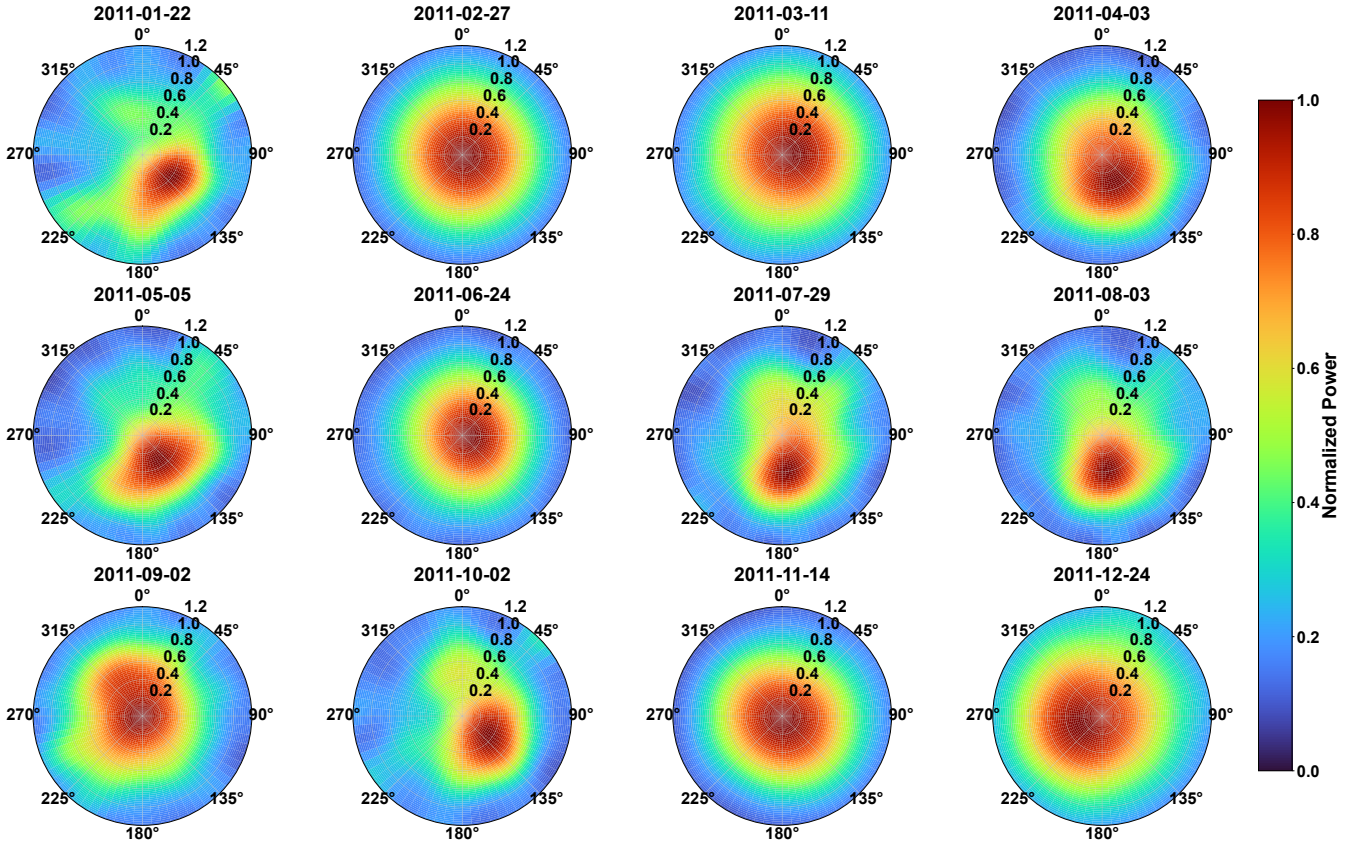


Figure S3. Monthly polar F–K power maps for the SPITS array in 2011 in the 0.5 Hz to 2.0 Hz band. Each panel represents one month and shows the day selected by maximum daily band power among available records. The radial axis is slowness ($\mathrm{s\,km^{-1}}$), and the angular axis is backazimuth (degrees, clockwise from north). The colour bar indicates normalized beam power (0–1). The maps are dominated by low-slowness energy and show month-to-month changes in azimuthal power distribution, indicating seasonal variability in dominant propagation directions.

S4 Near-array wind

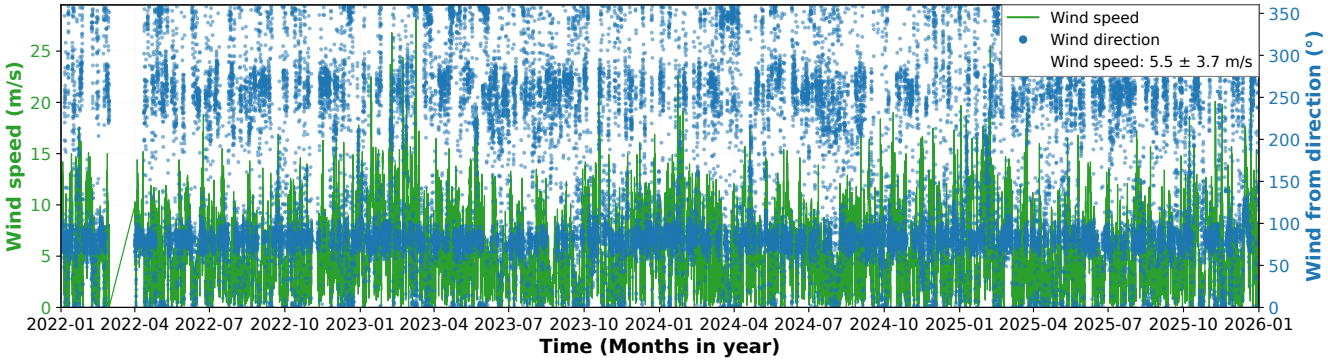


Figure S4. Hourly wind at Janssonhaugen Vest (SN99874) for 2022–2025. Wind speed (green) and wind-from direction (blue dots) are shown on a shared time axis. The legend reports the mean ± one standard deviation of wind speed; no mean wind direction is shown. Vertical gaps indicate periods without meteorological data.

S5 SPITS data availability

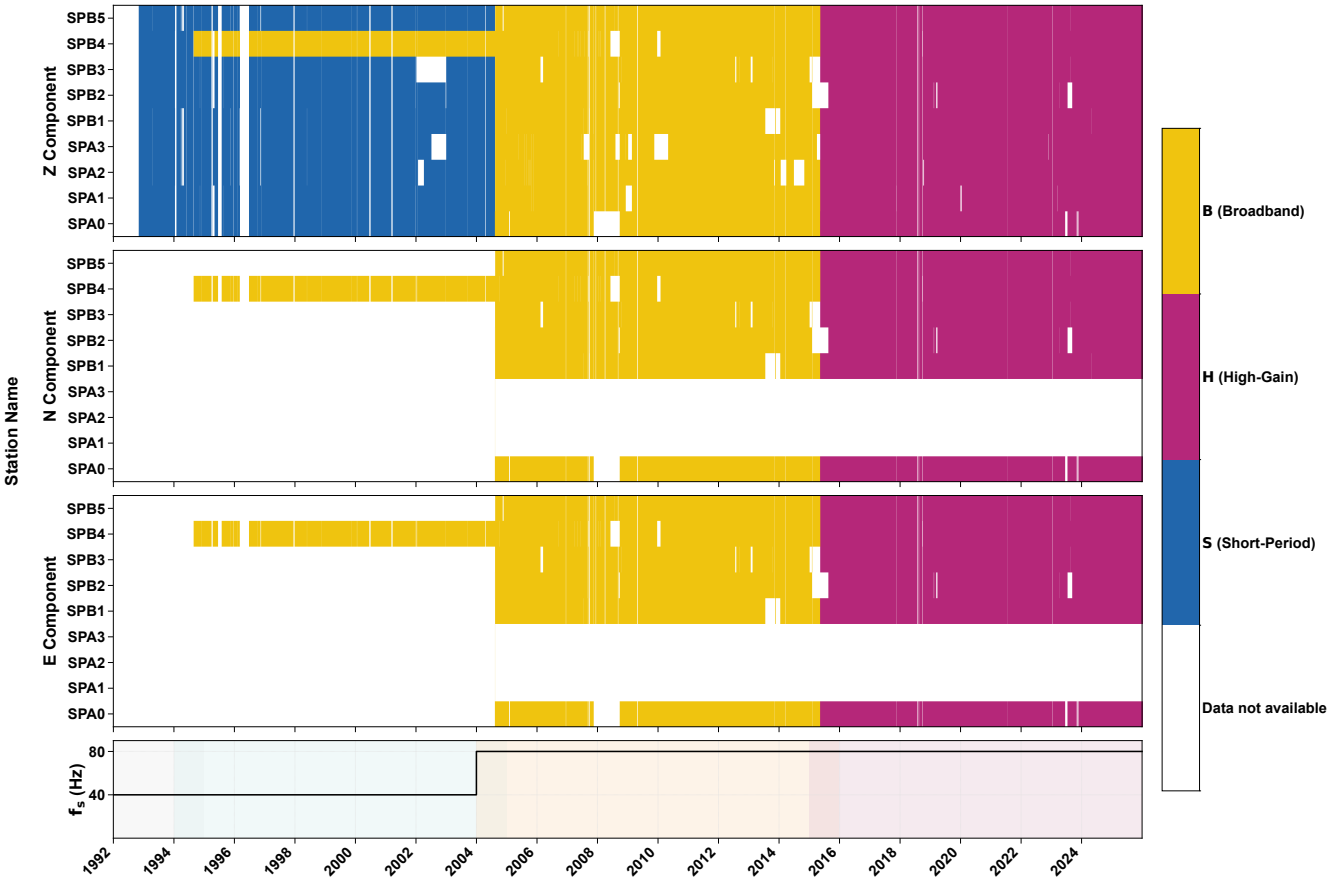


Figure S5. Long-term data availability and instrument configuration of the SPITS seismic array. The top three panels show, for the Z, N and E components respectively, the temporal availability of continuous waveform data for each SPITS station (vertical axis) from 1992 to 2025 (horizontal axis). Each coloured pixel denotes at least one day of usable data for the corresponding station, component and year; white intervals indicate gaps with no data. The colour encodes the deployed sensor class: S (short-period) instruments in blue, H (high-gain) instruments in magenta, and B (broadband) instruments in yellow, as indicated by the colour bar on the right. The bottom panel summarises the evolution of the nominal sampling rate f_s of the array, highlighting the stepwise upgrades from the initial configuration to 40 Hz and finally 80 Hz, with lightly shaded bands marking the different acquisition epochs.

S6 Waveform coherence and stacking convergence

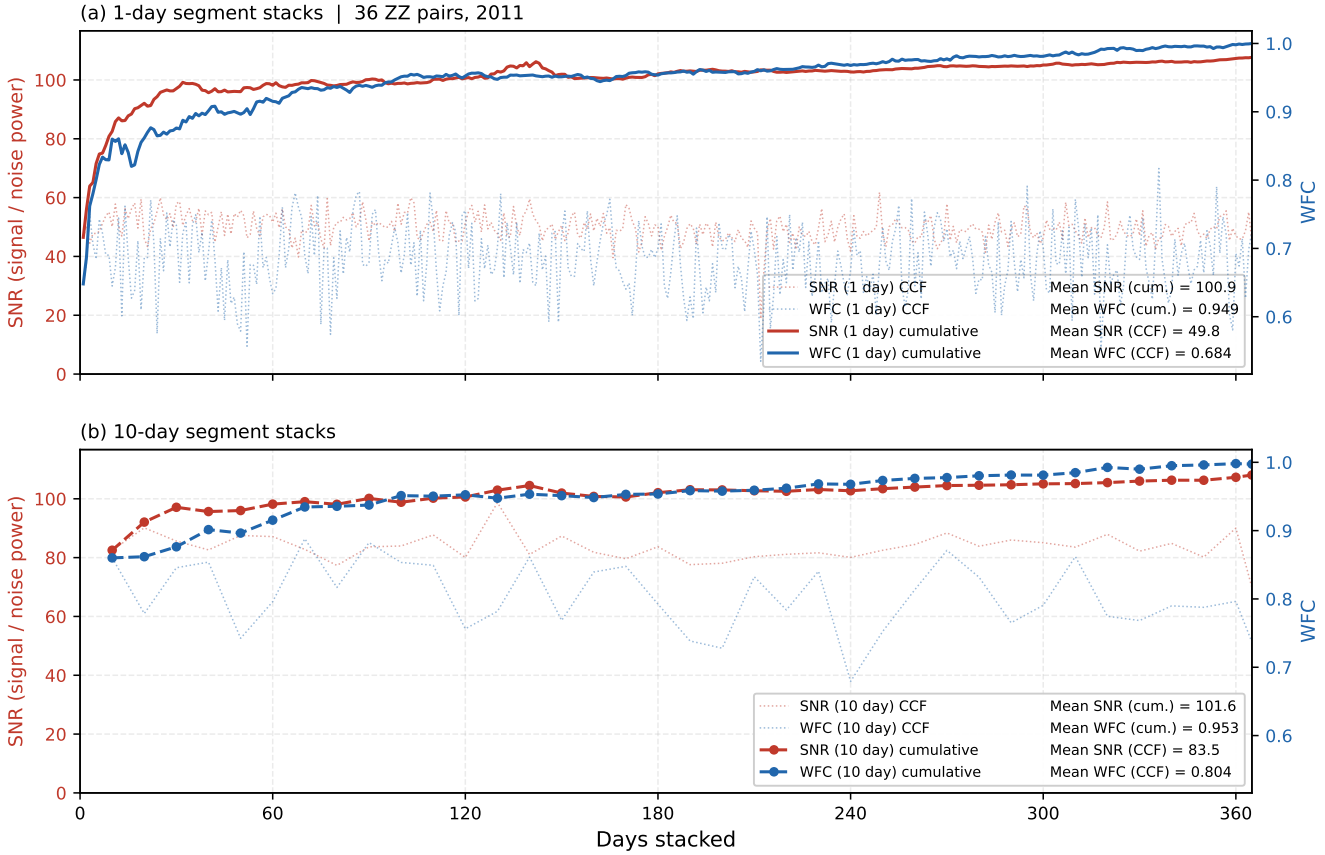


Figure S6. Comparison of 1-day versus 10-day segment stacks using waveform coherence (WFC, blue, right axis) and signal-to-noise ratio (SNR, red, left axis) for 36 inter-station ZZ pairs in 2011. Dotted curves are the metrics of each CCF against the full-year linear reference; solid/dashed curves are the running linear stack of those CCFs. **(a)** Daily segment-averaged CCFs. **(b)** Non-overlapping 10-day means of the same daily CCFs, then stacked. This figure compares stack quality; daily CCFs remain the input for dv/v in the main text.

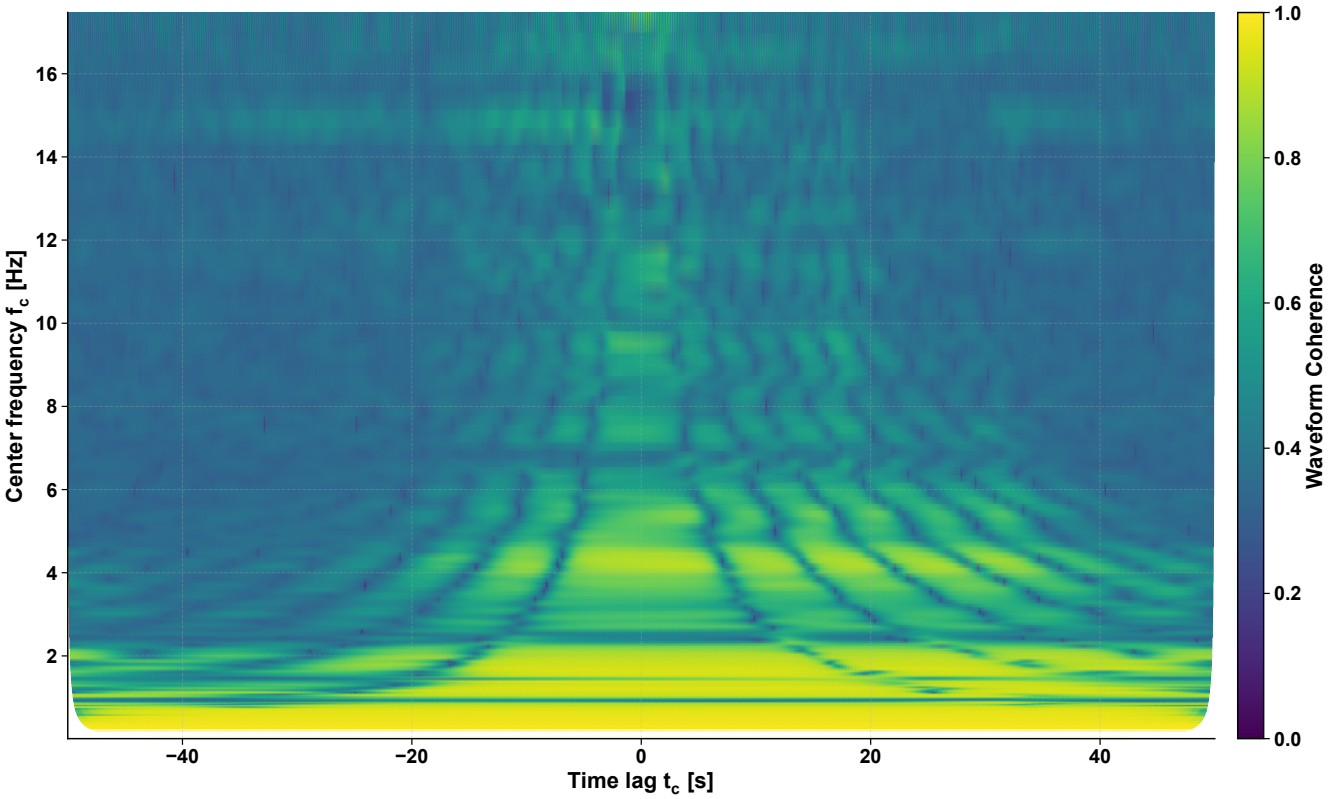


Figure S7. Waveform coherence $W(f_c, \tau)$ as a function of centre frequency f_c and time lag τ for the vertical (ZZ) inter-station pair SPB3–SPB5, computed from one year (2011) of daily CCFs. The colour scale indicates coherence from 0 (low) to 1 (high). Coherence persists to longer lags at lower frequencies and becomes confined to shorter lags at higher frequencies, consistent with frequency-dependent coda duration; the plot is used to guide selection of stable monitoring bands.

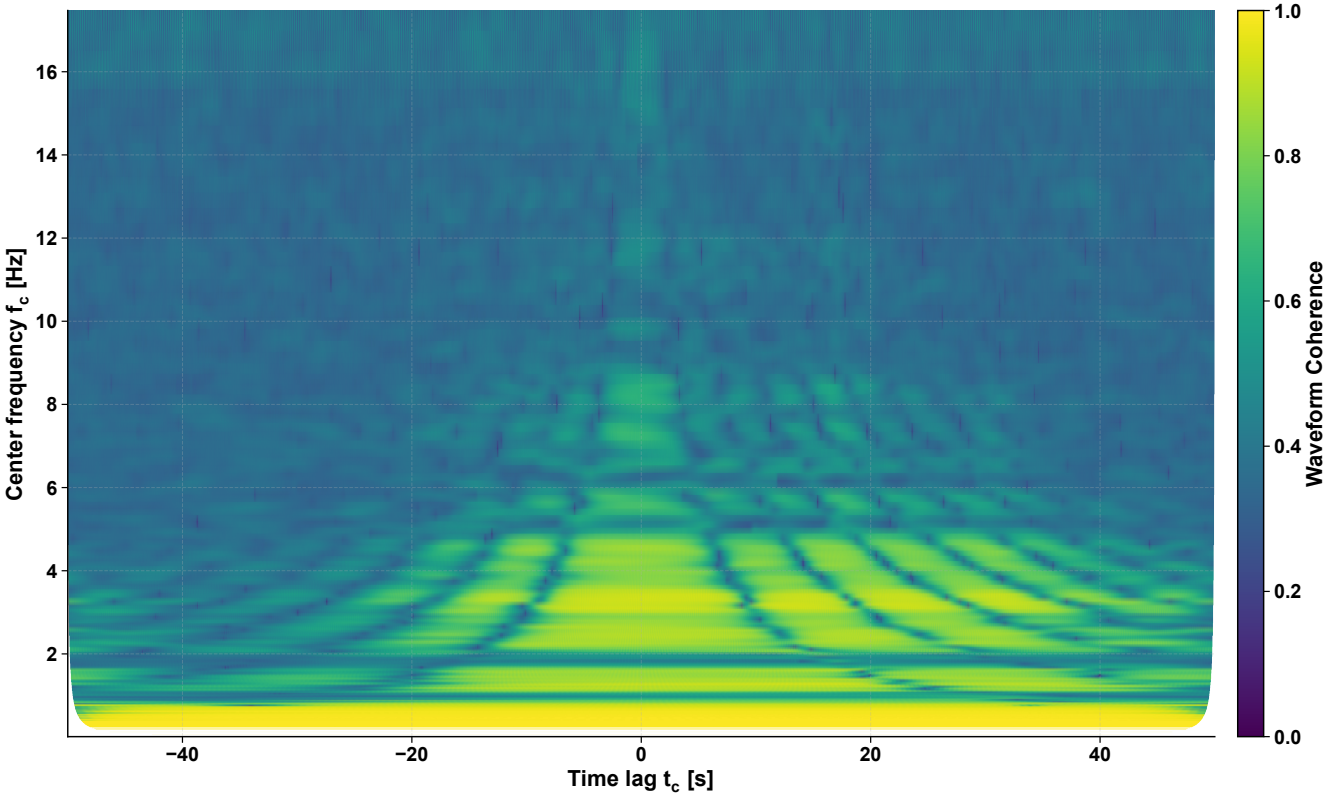


Figure S8. CCF waveform coherence $W(f_c, \tau)$ as a function of centre frequency f_c and time lag τ for the horizontal (NN) inter-station pair SPB1–SPB4, computed from one year (2020) of daily CCFs. The colour scale indicates coherence from 0 (low) to 1 (high). As for the vertical component, coherence persists to longer lags at lower frequencies and becomes confined to shorter lags at higher frequencies.

S7 Stacking method comparison

The Selective stack is shown in the main text. Figures S8–S10 give the Robust, PWS, and tf-PWS comparisons for the same station pair and year. As in the main-text stacking figure, the middle panel mutes the direct arrival ($|\tau| < 8$ s) and is scaled to the coda window.

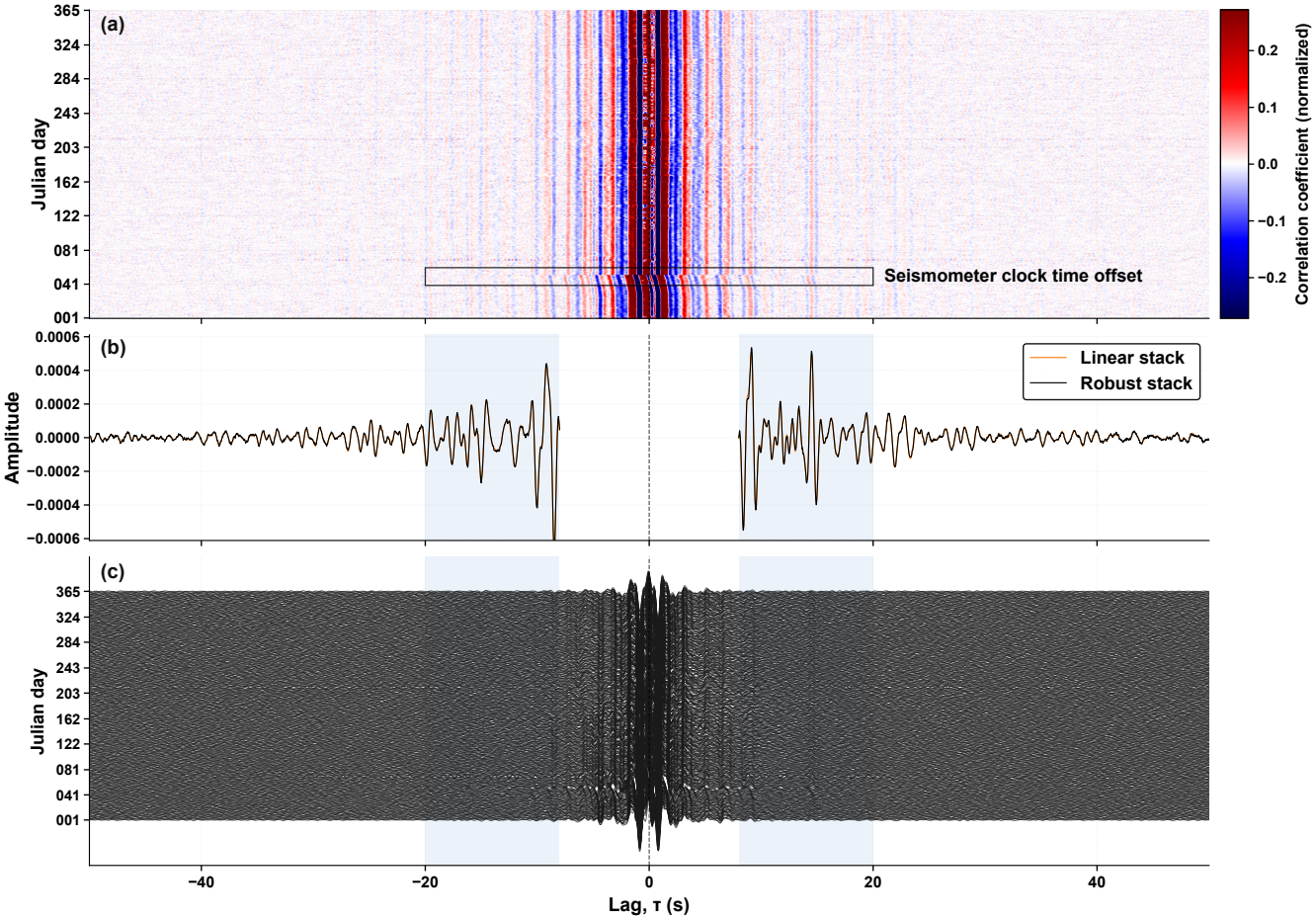


Figure S9. Daily cross-correlations and stacking: Robust stack. Station pair SPB3–SPB5, 2011 (0.5 Hz to 2.0 Hz). In the stack panel the direct arrival ($|\tau| < 8$ s) is muted and traces are scaled to the coda.

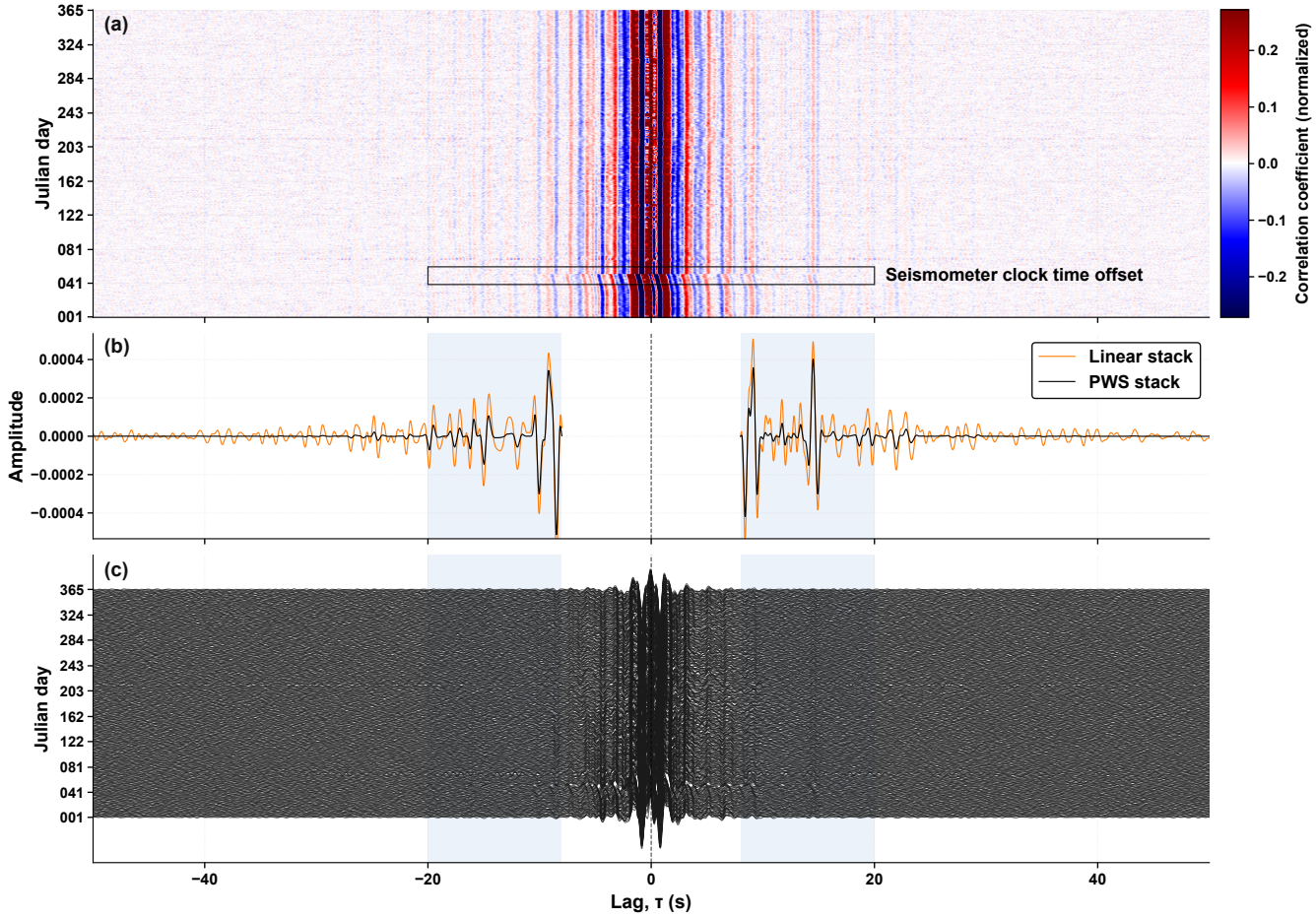


Figure S10. Daily cross-correlations and stacking: Phase-Weighted Stack (PWS). Station pair SPB3–SPB5, 2011 (0.5 Hz to 2.0 Hz). In the stack panel the direct arrival ($|\tau| < 8$ s) is muted and traces are scaled to the coda.

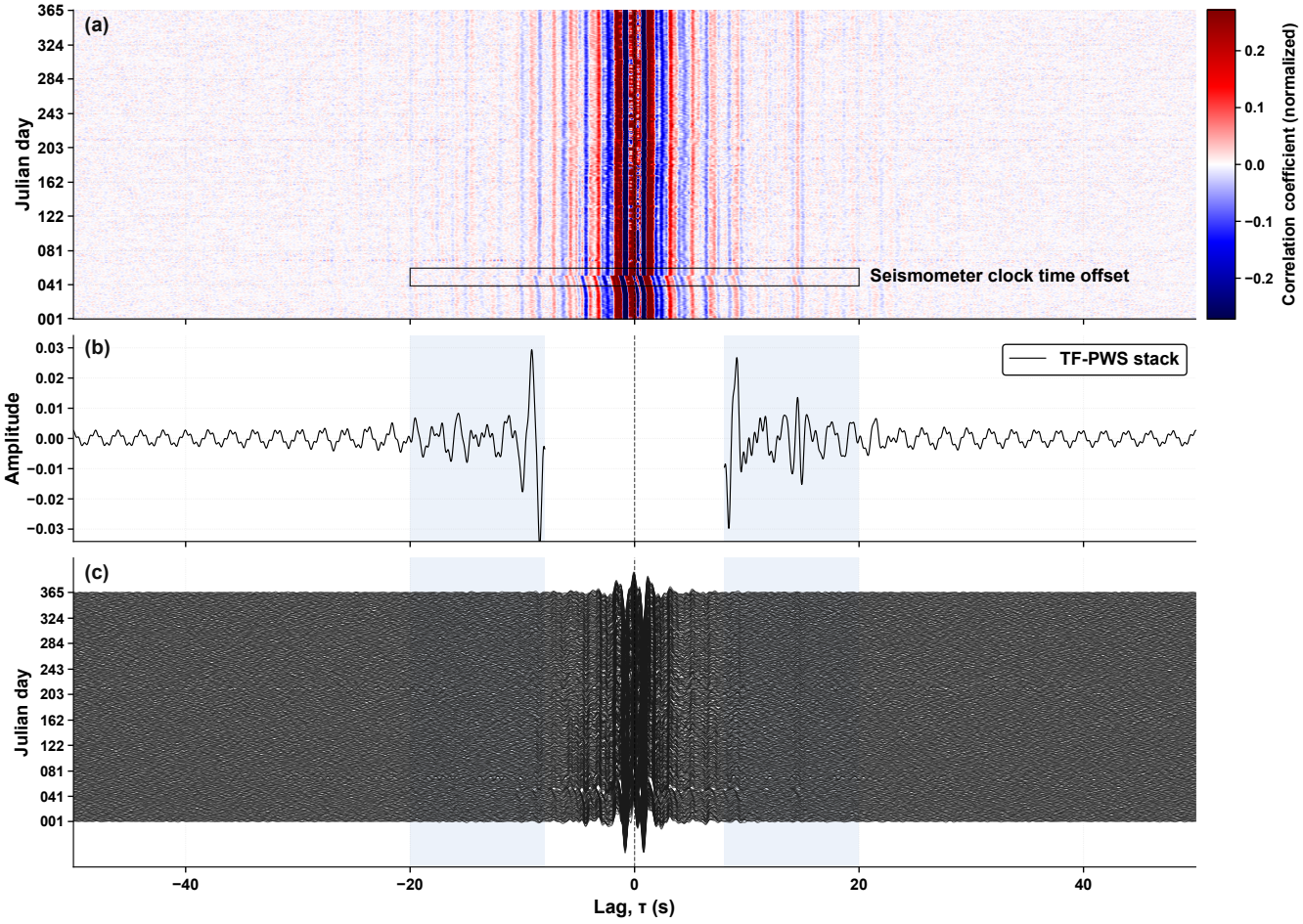


Figure S11. Daily cross-correlations and stacking: time-frequency Phase-Weighted Stack (tf-PWS). Station pair SPB3–SPB5, 2011 (0.5 Hz to 2.0 Hz). In the stack panel the direct arrival ($|\tau| < 8$ s) is muted and traces are scaled to the coda.

S8 Gaussianity and stationarity of the coda

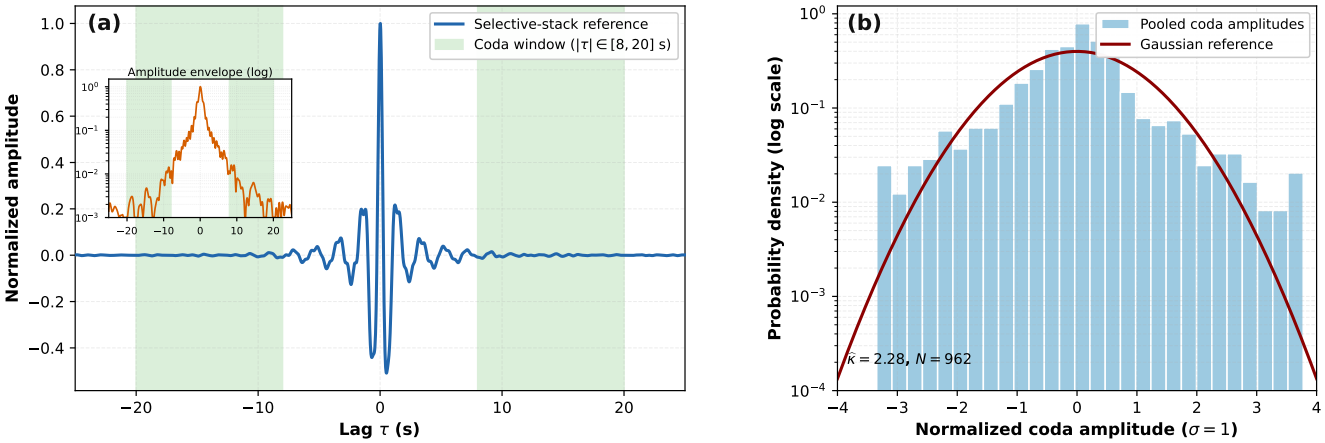


Figure S12. Full-year Selective-stack reference and coda amplitude distribution. **(a)** Array-mean Selective-stack reference over 36 pairs; green bands mark the coda window $|\tau| \in [t_{\min}, t_{\max}]$. The inset shows the amplitude envelope on a logarithmic axis, which decays with lag, so the coda is not amplitude-stationary. **(b)** Probability density (log axis) of the $N = 962$ pooled coda amplitudes versus a standard Gaussian; the distribution is leptokurtic, with unbiased excess kurtosis $\widehat{\kappa} \approx 2.3$.

S9 ZZ velocity variations from 10-day stacks

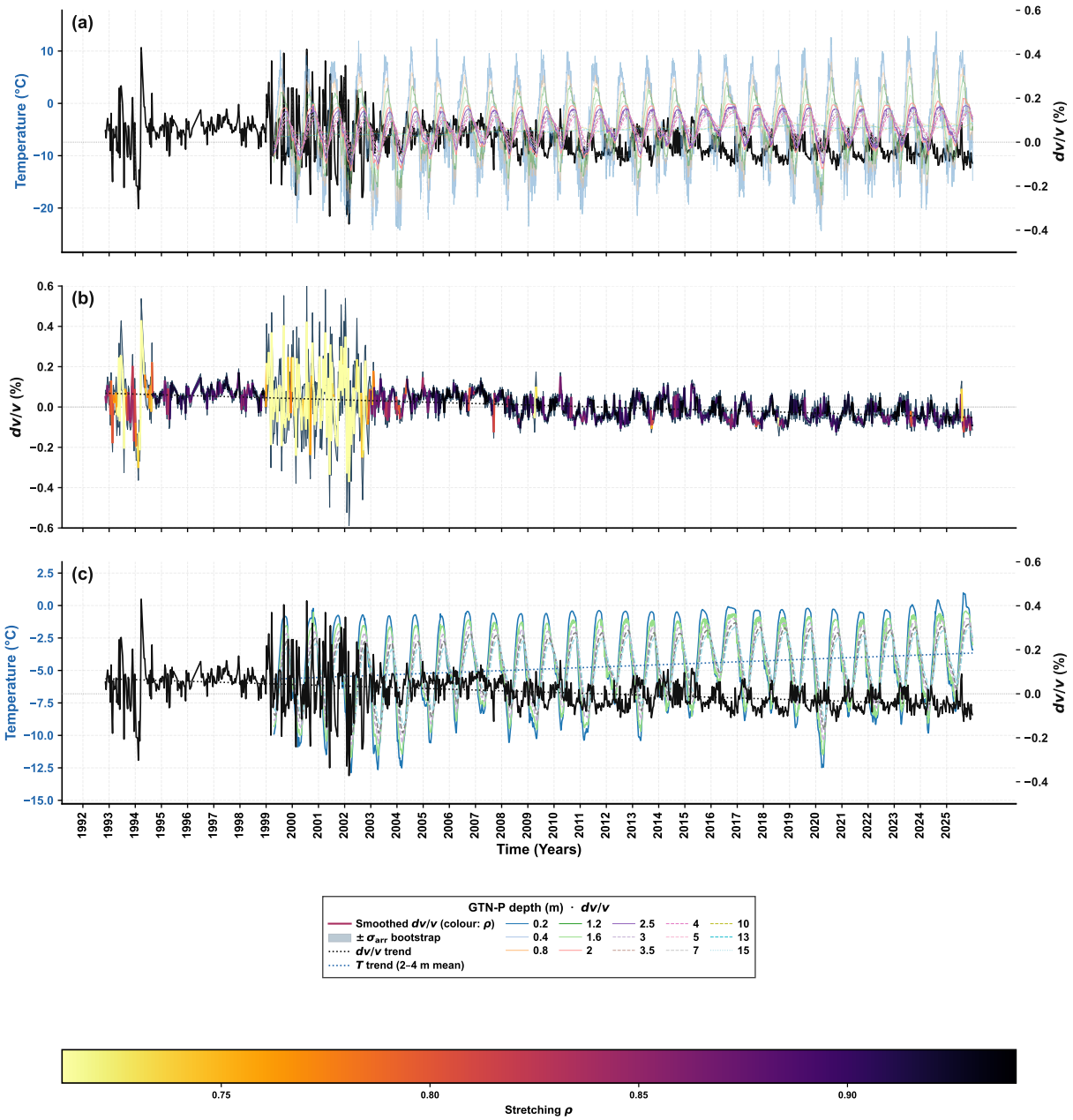


Figure S13. Array-averaged inter-station ZZ dv/v estimated from 10-day stacks, compared with GTN-P soil temperatures at Janssonhaugen (1992–2025). The panels follow the main-text ZZ figure, which uses daily stacks. **(a)** Smoothed dv/v against soil temperature at all GTN-P depths (dual axis). **(b)** Smoothed dv/v coloured by stretching correlation coefficient ρ, with bootstrap uncertainty and linear trend. **(c)** Soil temperature at 2 m to 4 m coloured by depth, with smoothed dv/v (dual axis) and trends. Daily stacks remain the series interpreted in the main text.

S10 Supporting dv/v products

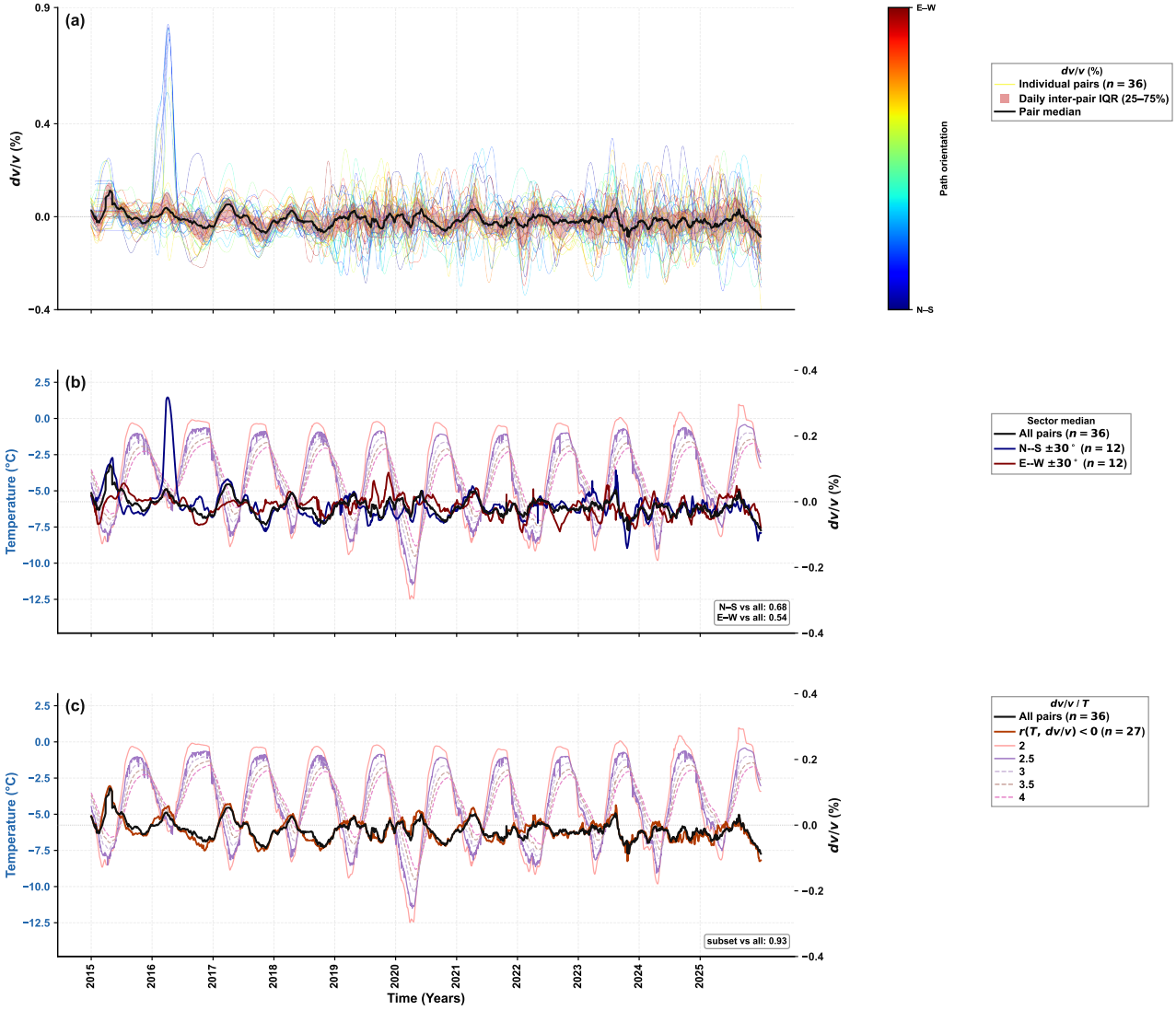


Figure S14. Per-pair inter-station ZZ dv/v (2015–2025). **(a)** Individual Gaussian-smoothed pair series coloured by path orientation (0° N–S, 90° E–W). The red band is the daily interquartile range (25th–75th percentiles) of the 36 pair estimates; the black line is their median. Temperature is omitted so the seasonal envelope is visible (dv/v axis from -0.4 to 0.9%). **(b)** Array medians for all pairs and for N–S and E–W sectors ($\pm 30°$), with GTN-P soil temperature at selected depths. Annotated values are Pearson r between each sector median and the 36-pair median. **(c)** All-pair median versus the subset of pairs with $r(T, dv/v) < 0$, again with soil temperature.

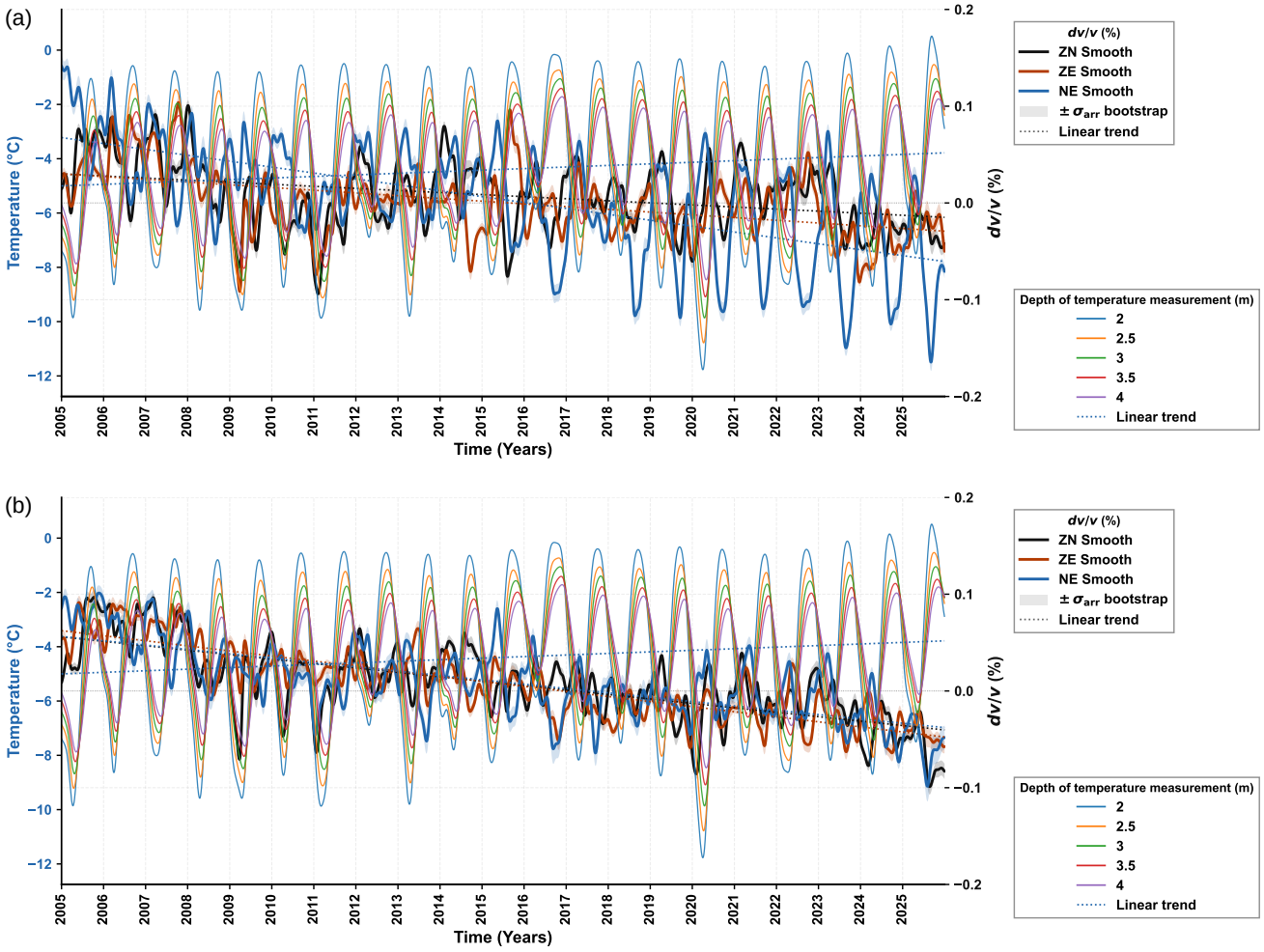


Figure S15. Comparison of array-averaged relative seismic velocity variations with GTN-P soil temperatures at Janssonhaugen for cross-component correlations. Top: single-station cross-correlations (ZN, ZE, and NE; 2005–2025) with soil temperature at $2\,\mathrm{m}$ to $4\,\mathrm{m}$ depth. Bottom: inter-station cross-correlations (ZN, ZE, and NE; 2005–2025), where daily dv/v is the array median over all contributing station pairs for each cross-component product. Gaussian-smoothed dv/v and soil temperature are compared with linear trends (see in-figure legend). Cross-component products are exploratory and complement the primary same-component ZZ analysis in the main text.

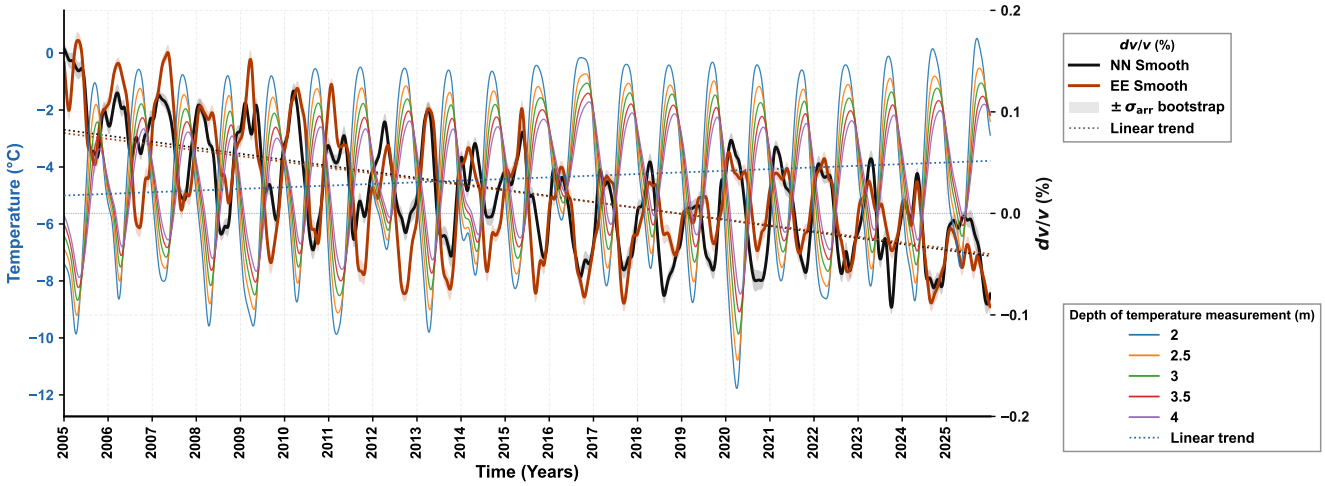


Figure S16. Array-averaged inter-station geographic NN and EE dv/v compared with GTN-P soil temperature at Janssonhaugen (2005–2025). Smoothed daily soil temperature (selected depths between 2 and 4 m), linear trends, and $\pm\sigma_{\mathrm{arr}}$ bootstrap uncertainty are shown (see in-figure legend).

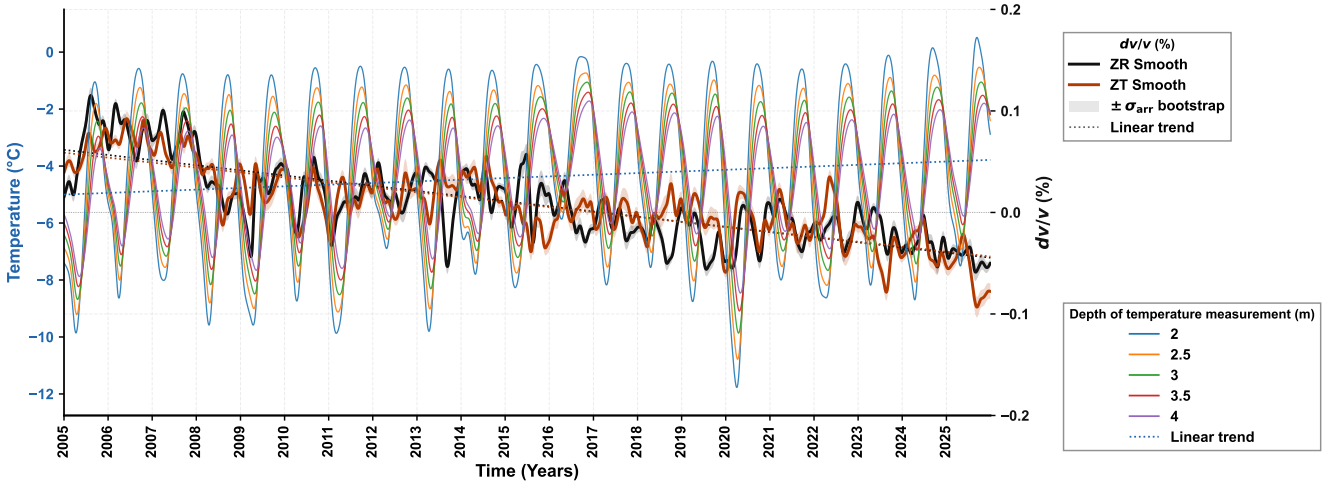


Figure S17. Array-averaged inter-station vertical–radial (ZR) and vertical–transverse (ZT) dv/v with GTN-P soil temperature at 2 m to 4 m depth (2005–2025). Gaussian-smoothed dv/v series are shown with linear trends and $\pm\sigma_{\mathrm{arr}}$ bootstrap uncertainty (see in-figure legend). Mixed vertical–horizontal products are treated as supporting checks on Rayleigh-type coupling in the pair-specific R/T frame.

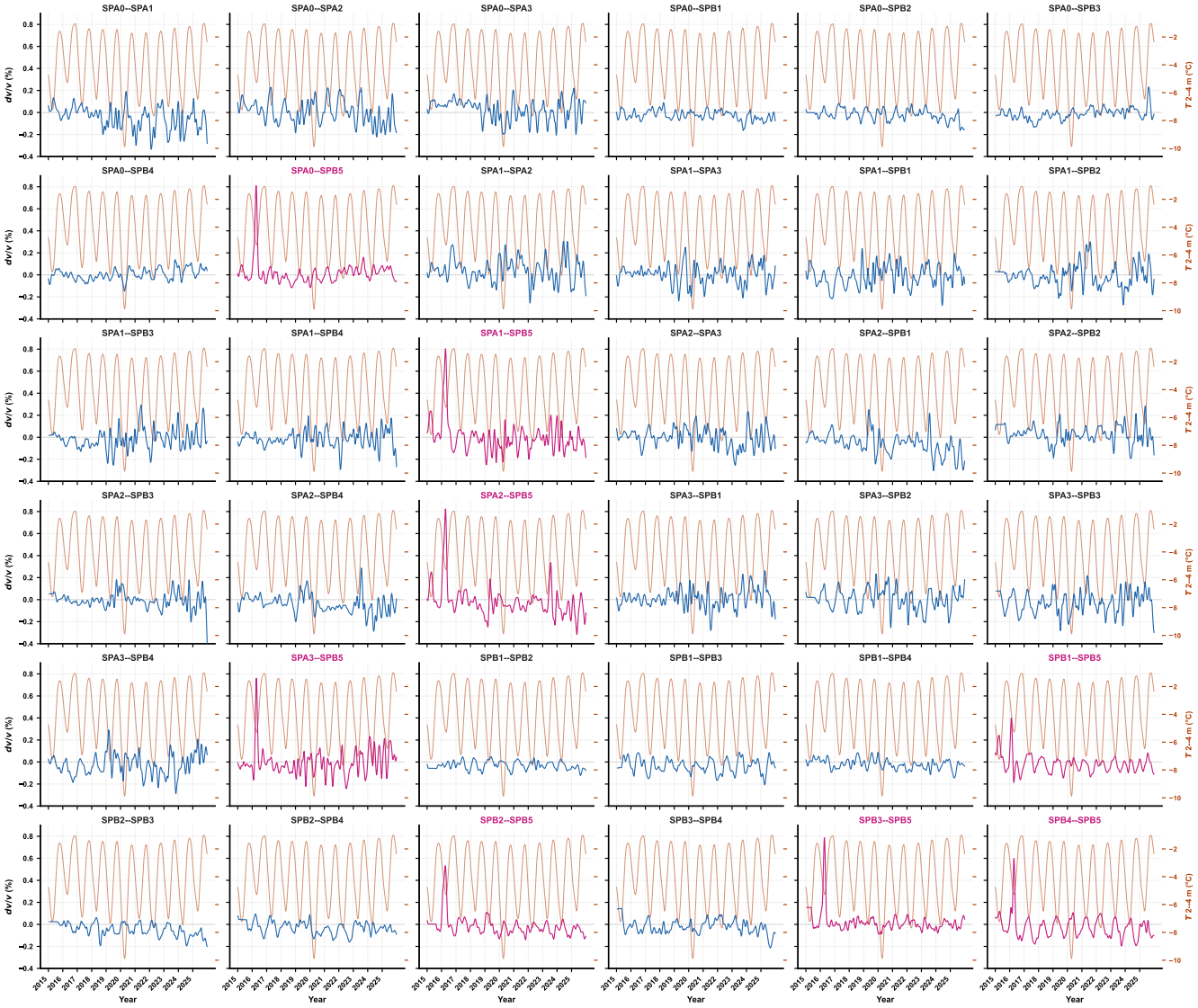


Figure S18. Individual inter-station ZZ dv/v pairs for 2015–2025 (one panel per pair), with mean GTN-P soil temperature at 2 m to 4 m (orange, right axis). Paths that include SPB5 are shown in magenta; all other pairs are blue. The 2016 positive excursion appears on every SPB5 path and is absent from the remaining pairs.

S11 Sensitivity to the stretching reference epoch

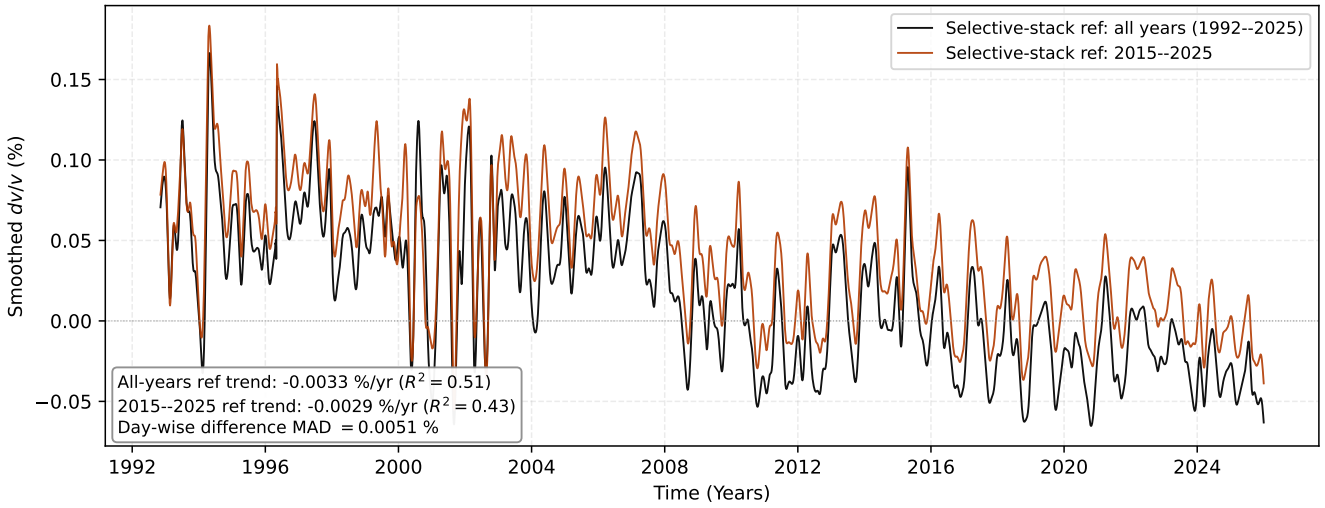


Figure S19. Sensitivity of array-median ZZ dv/v to the Selective-stack reference epoch used for stretching. Gaussian-smoothed array-median dv/v when each daily CCF is stretched against an all-years Selective-stack reference (1992–2025; black) versus a recent-years reference (2015–2025; orange). Annotated rates are ordinary-least-squares trends of the smoothed series; the day-wise difference MAD quantifies the residual offset. The seasonal cycle and the sign of the long-term trend are preserved; absolute dv/v levels differ because the reference defines the zero of the relative-velocity scale.